A

Addition of Multiple Coherent Waves

There are many instances throughout the text where the simplification of a sum of coherent sine and cosine terms is necessary. Sine and cosine terms that are coherent have the same oscillatory frequency ωt but may have different amplitudes and phases. These waves can be combined into a single sine, cosine, or complex exponential expression. This appendix shows how to make the reductions.

A sum of N coherent exponentials is

$$S = \sum_{n=1}^{N} a_n \mathrm{e}^{j(\omega t \pm \phi_n)} \tag{A.1}$$

Expanding the sum makes

$$\begin{aligned} \sum a_n \mathrm{e}^{\pm j\phi_n} &= \sum a_n \cos\phi_n \pm j \sum a_n \sin\phi_n \\ &= A \pm jB \end{aligned} \tag{A.2}$$

where,

$$A = \sum_{n=1}^{N} a_n \cos\phi_n \ , \quad B = \sum_{n=1}^{N} a_n \sin\phi_n$$

Converting to polar form, the sum S simplifies to

$$\sum_{n=1}^{N} a_n \mathrm{e}^{j(\omega t \pm \phi_n)} = \sqrt{A^2 + B^2}\ \exp\left(j(\omega t \pm \tan^{-1}(B/A))\right) \tag{A.3}$$

The simplifications for sine and cosine sums requires an additional step of exponential expansion. Thus, with

$$S' = \sum_{n=1}^{N} a_n \sin(\omega t - \phi_n) \ , \tag{A.4}$$

Table A.1. Identities for Coherent Wave Addition

$$\sum_{n=1}^{N} a_n \mathrm{e}^{j(\omega t \pm \phi_n)} = \sqrt{A^2 + B^2}\ \exp\left(j(\omega t \pm \tan^{-1} B/A)\right)$$

$$\sum_{n=1}^{N} a_n \sin(\omega t \pm \phi_n) = \sqrt{A^2 + B^2}\ \sin\left(\omega t \pm \tan^{-1}(B/A)\right)$$

$$\sum_{n=1}^{N} a_n \cos(\omega t \pm \phi_n) = \sqrt{A^2 + B^2}\ \cos\left(\omega t \mp \tan^{-1}(B/A)\right)$$

$$\text{where } A = \sum_{n=1}^{N} a_n \cos\phi_n, \quad B = \sum_{n=1}^{N} a_n \sin\phi_n$$

exponential expansion of the sine terms yields

$$S' = \frac{1}{2j}\ \left\{ \mathrm{e}^{j\omega t} \sum a_n \mathrm{e}^{-j\phi_n} - \mathrm{e}^{-j\omega t} \sum a_n \mathrm{e}^{j\phi_n} \right\} \tag{A.5}$$

Substitution of (A.2) into (A.5) yields

$$\begin{aligned} S' &= \frac{1}{2j}\ \left\{ A\left(\mathrm{e}^{j\omega t} - \mathrm{e}^{-j\omega t}\right) - jB\left(\mathrm{e}^{j\omega t} + \mathrm{e}^{-j\omega t}\right) \right\} \\ &= A\sin\omega t - B\cos\omega t \end{aligned} \tag{A.6}$$

Recognizing that (A.6) is similar to the equation for an ellipse, the final simplification produces

$$\sum_{n=1}^{N} a_n \sin(\omega t \pm \phi_n)\ = \sqrt{A^2 + B^2}\ \sin\left(\omega t \pm \tan^{-1} B/A\right) \tag{A.7}$$

In an analogous way, a sum of coherent cosine terms simplifies to

$$\sum_{n=1}^{N} a_n \cos(\omega t \pm \phi_n)\ = \sqrt{A^2 + B^2}\ \cos\left(\omega t \mp \tan^{-1} B/A\right) \tag{A.8}$$

Table (A.1) summarizes the results.

B

Select Magnetic Field Profiles

Non-latching iron garnet Faraday rotation elements require the presence of an external magnetic field to saturate the magnetic domains. To generate the Faraday effect, the field lines are aligned predominantly in the direction of optical propagation. A cylindrical magnet with the center bore gives the required field profile and is also simple to analyze. This appendix gives analytic and semi-analytic expressions for the field along the centerline of the bore and in the plane perpendicular to the propagation direction, where the plane is located half-way along the bore.

A permanent magnet is described by a magnetic dipole distribution within the material and a magneto-quasi-static magnetic field. The relevant form of Maxwell's equations are then

$$\nabla \times \mathbf{H} = 0 \tag{B.1a}$$

$$\nabla \cdot \mu_o \mathbf{H} = -\nabla \cdot \mu_o \mathbf{M} \tag{B.1b}$$

Since the magnetic field is irrotational, the field can be defined as the gradient of a scalar potential (cf. 1.2.2b):

$$\mathbf{H} = -\nabla \Psi \tag{B.2}$$

where Ψ is the scalar magnetic potential. Definition of the magnetic charge density ρ_m as

$$\rho_m = -\nabla \cdot \mu_o \mathbf{M} \tag{B.3}$$

and substitution of (B.2) into (B.1b) yields Poisson's equation

$$\nabla^2 \Psi = -\frac{\rho_m}{\mu_o} \tag{B.4}$$

A solution to Poisson's equation is the superposition integral

$$\Psi = \int_{V'} \frac{\rho_m(\mathbf{r}')}{4\pi\mu_o |\mathbf{r} - \mathbf{r}'|} \, dV' \tag{B.5}$$

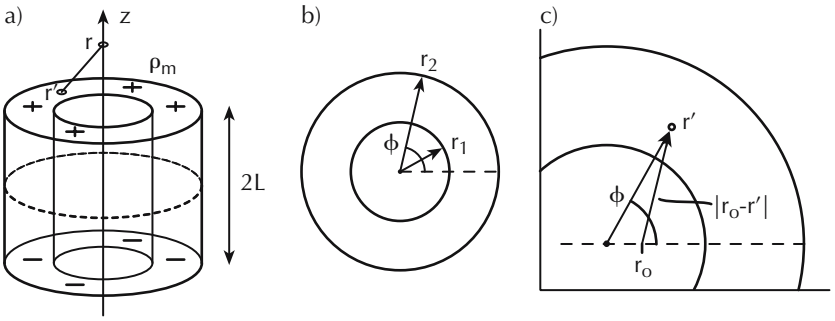

Fig. B.1. Geometry of cylindrical magnet. a) Cylindrical magnet with center bore. Magnetic charges lie on the top and bottom annular surfaces. b) Top view showing inner and outer radius. c) For in-plane calculation, position r_o is offset from the z-axis an can be related to angle ϕ (see text).

where the prime denotes a point on or within the magnetic medium and $\mathbf{r}$ is a spatial coordinate. The integral is taken over the volume of the magnetic solid. Figure B.1 illustrates the magnetic cylinder under consideration. Taking advantage of the cylindrical symmetry, the superposition integral is evaluated as

$$\Psi = \int_o^{2\pi} d\phi \int_{r1}^{r2} r' dr' \int_{-L}^{L} dz \frac{\rho_m(\mathbf{r}')}{4\pi\mu_o|\mathbf{r} - \mathbf{r}'|} \tag{B.6}$$

The first evaluation of (B.6) is done along the z-axis. Integration of (B.6) along z yields two magnetic sheets, one annulus at $+L$ with positive "charges" $\mu_o M$ and the other annulus at $-L$ with negative charges $-\mu_o M$. Moreover, the distance from any point on the annular sheets to the z-axis is $|\mathbf{r} - \mathbf{r}'| = \sqrt{r'^2 + (z \mp L)^2}$, where the minus sign corresponds to the top sheet. The scalar potential, still in integral form, is

$$\Psi = \int_{r1}^{r2} \frac{2\pi\mu_o M r' dr'}{4\pi\mu_o\sqrt{r'^2 + (z - L)^2}} - \int_{r1}^{r2} \frac{2\pi\mu_o M r' dr'}{4\pi\mu_o\sqrt{r'^2 + (z + L)^2}} \tag{B.7}$$

Integration and subsequently taking the gradient as prescribed by (B.2) yields the magnetic field strength along the central axis [1, 2]:

$$\begin{aligned} H_z(z) \;=\; & -\frac{M}{2}\left((z - L)\left[\frac{1}{\sqrt{(z - L)^2 + r_2^2}} - \frac{1}{\sqrt{(z - L)^2 + r_1^2}}\right] - \right. \\ & \left. (z + L)\left[\frac{1}{\sqrt{(z + L)^2 + r_2^2}} - \frac{1}{\sqrt{(z + L)^2 + r_1^2}}\right]\right) \end{aligned} \tag{B.8}$$

Figure B.2(a) illustrates an evaluation of (B.8). A design goal would be to achieve the highest possible magnetic field in the region of $z = 0$ while minimizing the size of the magnet. The change in sign is due to the fields wrapping around either magnet end to terminate on the surface charges.

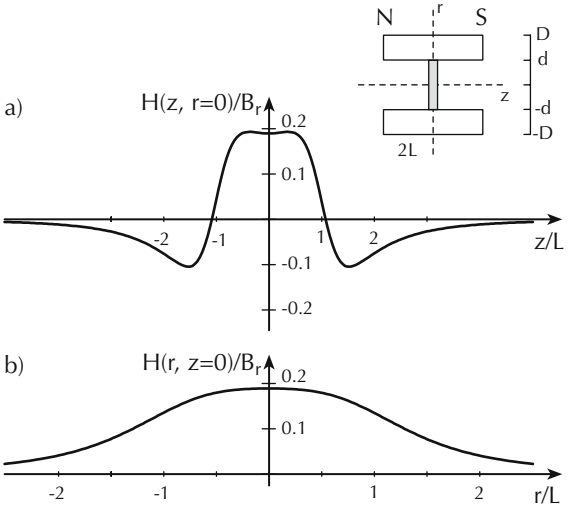

Fig. B.2. Axial and transverse magnetic field amplitude H_z of a cylindrical magnet. a) Axial field strength of H_z under the conditions $r_2 = L$ and $r_1 = L/2$. b) Transverse field strength of H_z in plane located at center of magnet. Inset shows coordinates.

The purpose of the following transverse field calculation is to explore the field uniformity within the bore but off-axis. Since an optical beam has finite width, it is insufficient to saturate the center of an iron garnet but not the outer edges. In order to keep the analysis quasi-analytic, only the field amplitude in a plane normal to z and located half-way along the bore is calculated.

The key to evaluating the superposition integral in this case is an analytic expression for $|\mathbf{r}' - \mathbf{r}|$ away from the z-axis. Referring to Fig. B.1(c), offset position r_o is related to r' and ϕ as

$$|r' - r_o| = \sqrt{\mathcal{R}^2 + (z \pm L)^2} \tag{B.9}$$

where the in-plane length is

$$\mathcal{R}^2 = (r' \sin\phi)^2 + (r' \cos\phi - r_o)^2 \tag{B.10}$$

With this measure, the superposition integral is

$$\Psi = \int_0^{2\pi} d\phi \int_{r_1}^{r_2} r' dr' \frac{\mu_o M}{4\pi\mu_o} \left[\frac{1}{\sqrt{\mathcal{R}^2 + (z+L)^2}} - \frac{1}{\sqrt{\mathcal{R}^2 + (z-L)^2}} \right] \tag{B.11}$$

Even though (B.11) does not have an analytic form, an expression closer to $H_z(r, z = 0)$ can still be found. In particular,

$$H_z = -\frac{\partial}{\partial z}\Psi \tag{B.12}$$

Carrying through the derivative with respect to z first and then setting $z = 0$ yields

$$H_z(r, z = 0) = \int_0^{2\pi} d\phi \int_{r_1}^{r_2} \frac{2\mu_o M}{4\pi\mu_o} \frac{r' dr'}{[\mathcal{R}^2 + 1]^{3/2}} \tag{B.13}$$

This integral can be evaluated numerically. Applying the parameters from Fig. B.2(a) to (B.13) generates the curve given in Fig. B.2(b). Note that the z component of the magnetic field does not change sign but monotonically decays to zero far away from the magnet. Also, the uniformity of the field, for these parameters, remains within 10% of the peak within the inner radius.

A samarium-cobalt (SmCo) magnet can be an excellent choice for the permanent around an iron garnet due to its high coercivity in a small size. Length-diameter products of 1 mm^2 can readily achieve the 100–250 Oe magnetic field required for H_{sat} in iron garnets.

References

1. H. A. Haus and J. R. Melcher, *Electromagnetic Fields and Energy.* Englewood Cliffs, New Jersey: Prentice–Hall, 1989.
2. K. Shiraishi, F. Tajima, and S. Kawakami, "Compact faraday rotator for an optical isolator using magnets arranged with alternating polarities," *Optics Letters*, vol. 11, no. 2, pp. 82–84, 1986.

C

Efficient Calculation of PMD Spectra

Scalar and vector PMD spectra calculated in the Stokes-based PMD representation is straightforward and efficient. The concatenation rules presented in §8.2.4 starting on page 337 are derived for $\vec{\tau}$ and $\vec{\tau}_\omega$ by taking frequency derivatives analytically; numerical derivatives are therefore not necessary.

This appendix gives a vectorized code fragment written in Matlab which can be used as a core calculator for larger programs. Given the particular vectorization that follows, the code works well when there are more frequency evaluations than birefringent segments.

The differential-group delay $|\vec{\tau}|$, magnitude second-order PMD $|\vec{\tau}_\omega|$, and polarization-dependent chromatic dispersion $|\vec{\tau}|_\omega$ scalar spectra are calculated for each frequency ω by

$$|\tau|^2 = \vec{\tau} \cdot \vec{\tau} \tag{C.1a}$$

$$|\tau_\omega|^2 = \vec{\tau}_\omega \cdot \vec{\tau}_\omega \tag{C.1b}$$

$$|\tau|_\omega = \frac{\vec{\tau} \cdot \vec{\tau}_\omega}{\sqrt{\vec{\tau} \cdot \vec{\tau}}} \tag{C.1c}$$

The output and input PSP vector spectra are

$$\hat{p}_{\text{out}} = \vec{\tau}/\tau \tag{C.2a}$$

$$\hat{p}_{\text{in}} = R^\dagger \hat{p}_{\text{out}} \tag{C.2b}$$

where $R = R_N R_{N-1} \ldots R_1$. Each rotation operator is expanded in vector form as

$$R_k = I \cos(\omega\tau_k) + (1 - \cos(\omega\tau_k))(\hat{r}_k \hat{r}_k \cdot) + \sin(\omega\tau_k)(\hat{r}_k \times) \tag{C.3}$$

where τ_k is the DGD of a single birefringent segment and $\hat{r}_k$ is the Stokes direction of its birefringent axis. The concatenation equations (8.2.34) on page 337 are used to compute the cumulative first- and second-order PMD vector.

```
function [tau2, tauw2, pdcd, PSPout, PSPin] = CalcPMDSpec_1(w_vec, r_vec, tau_vec, phz_vec)

%          Inputs:
%          /w_vec/    (Trad/s) 1 x wlen vector of radial frequency range
%          /r_vec/    ( scalar ) 3 x Nseg matrix, each column is a unit Stokes vector of tau_k
%          /tau_vec/  (ps)     1 x Nseg vector of DGD for each segment
%                                 (not to be confused with the PMD vector tau)
%          /phz_vec/  (rad)    1 x Nseg vector of residual birefringent phase
%                                 for each segment.
%
%          Outputs:
%          /tau2/     (ps^2)    1 x wlen vector of DGD^2(w)
%          /tauw2/    (ps^4)    1 x wlen vector of SOPMD^2(w)
%          /pdcd/     (ps^2)    1 x wlen vector of PDCD(w)
%          /PSPout/ ( scalar )  3 x wlen matrix of output PSP Stokes vectors
%          /PSPin/  ( scalar )  3 x wlen matrix of input PSP Stokes vectors

% Defs
DEG2RAD = pi / 180; RAD2DEG = 180 / pi;
I2 = diag([1,1]);
I3 = diag([1,1,1]);

% Input-specific Defs
wlen = length(w_vec);
Nseg = length(tau_vec);

% Calculate rrdot and rcross for each segment up front
% Note: rrdot and rcross matrix has the following structure:
%
%  rrdot_vec = [rrdot(1) rrdot (2) ... rrrdot(Nseg)]
%                        ^
%                        |
%                        im
%
% where each rrdot is a 3x3 matrix itself. Same with rcross.
%

% Calculate rrdot and rcross for each segment
for k = 1: Nseg,

    im = 3 * (k - 1) + 1;                          % column index into rrdot_vec
    rrdot_vec(:, [0:2]+im) = r_vec(:,k) * r_vec(:,k)'; % rrdot from dyadic

    % rcross is sum over cross-products of r_vec w/ S1, S2, and S3
    for i = 1: 3,
        rcross_vec(:, (i-1)+im) = cross(r_vec(:,k), I3(:,i));
    end
end

% Precalculate the trig tables, row -> segment #; column -> freq
coswt = cos(tau_vec' * w_vec + phz_vec' * ones(size(w_vec)));
sinwt = sin(tau_vec' * w_vec + phz_vec' * ones(size(w_vec)));

% Define the tau vectors
for k = 1: Nseg,
    tauvec(:,k) = tau_vec(k) * r_vec(:,k);
end
```

```
% Now calculate the frequency response
for iw = 1: wlen,

    % Set the frequency for the concat
    w = w_vec(iw);

    % Initialize cumulative tau and tauw vectors.
    tau_cat = tauvec(:, 1);                 % tau(1) = tau_1
    tauw_cat = zeros(size(tauvec(:, 1)));  % tauw(1) = 0;

    % Initialize cumulative R operator
    R_cat = I3;

    % We need R1 to find PSPin
    Rseg = coswt(1, iw) * I3 + ...
        (1-coswt(1, iw)) * rrdot_vec(:, [0:2]+1) + ...
        sinwt(1, iw) * rcross_vec(:, [0:2]+1);

    % Make first concatenation
    R_cat = Rseg * R_cat;

    % Accumulate tau, tauw, and Rseg through each segment
    for iseg = 2: Nseg,

        % column index into rrdot_vec and rcross_vec
        im = 3 * (iseg - 1) + 1;

        % Construct R_iseg(w)
        Rseg = coswt(iseg, iw) * I3 + ...
               (1-coswt(iseg, iw)) * rrdot_vec(:, [0:2]+im) + ...
               sinwt(iseg, iw) * rcross_vec(:, [0:2]+im);

        % Accumulate R
        R_cat = Rseg * R_cat;

        % Accumulate tau_cat
        tau_cat = tauvec(:,iseg) + Rseg * tau_cat;

        % Accumulate tauw_cat
        tauw_cat = cross( tauvec(:,iseg), tau_cat ) + Rseg * tauw_cat;

    end

    % Calculate the input PMD vectors tau and tauw
    Radj = conj( transpose( R_cat ) );
    tau_in = Radj * tau_cat;
    tauw_in = Radj * tauw_cat;

    % Calculate scalar spectra (could do this outside the loop, too)
    tau2(iw) = tau_cat' * tau_cat;
    tauw2(iw) = tauw_cat' * tauw_cat;
    dgd = sqrt(tau2(iw));
    pdcd(iw) = tau_cat' * tauw_cat / dgd;

    % Calculate the vector spectra
    PSPout(:, iw) = tau_cat / dgd;
    PSPin(:, iw) = tau_in / dgd;

end
```

The point-of-view of the preceding code is that operators $\hat{r}_k\hat{r}_k\cdot$ and $\hat{r}_k\times$ as well as the $\omega\tau_k$ product can be evaluated outside the main loop. In this way the core loop is mainly a multiply-and-accumulate register.

After an initial setup, the operators $\hat{r}_k\hat{r}_k\cdot$ and $\hat{r}_k\times$ are evaluated for each PMD segment in the loop between `lines 39-48`.

`line 42:` $$(\hat{r}_k\hat{r}_k\cdot) = \hat{r}_k\hat{r}_k^T$$

`lines 45-47:` $$(\hat{r}_k\times) = \hat{r}_k \times \hat{s}_1 + \hat{r}_k \times \hat{s}_2 + \hat{r}_k \times \hat{s}_3$$

Matrices `rrdot_vec` and `rcross_vec` store the 3×3 operator associated with the k^{th} segment in a $3 \times 3k$ matrix that is indexed as a row vector on k.

The sine and cosine of the $\omega\tau_k$ product are computed before the concatenation loop. These calculations are stored in tables `coswt` and `sinwt` on `lines 51-52`. There is an important point that needs to be highlighted. Strictly speaking, the birefringent phase of a segment is $\omega\tau_k$. The radial frequency can certainly be used, such as $(2\pi)194.1$ THz. As an alternative, the birefringent phase of a segment is written $(\omega - \omega_o)\tau_k + \phi_k$, where ω_o is an arbitrary frequency and ϕ_k is a measure of the residual birefringent phase at ω_o. This form is useful when investigating the role of the birefringent phase on a PMD spectrum. The trigonometric terms on `lines 51-52` provide for a vector of residual birefringent phases that are added to $\omega\tau_k$, which if the vector is nonzero should be interpreted as $(\omega - \omega_o)\tau_k + \phi_k$.

Finally, the segment PMD vectors $\vec{\tau}_k$ are calculated in advance:

`lines 55-57:` $$\vec{\tau}_k = \tau_k\hat{r}_k$$

The main frequency loop runs from `lines 60-118`. For each frequency the respective `coswt` and `sinwt` values are recalled, the R_k operators are constructed, vectors $\vec{\tau}$ and $\vec{\tau}_\omega$ are calculated, and the scalar and vector PMD spectra are computed and stored. The vectors $\vec{\tau}$ and $\vec{\tau}_\omega$ are generated by the nested loop that runs from `lines 82-101`; this loop runs the concatenation equations (8.2.34) on page 337. The inner loop is initialized with

`lines 67-68:` $$\vec{\tau}(1) = \vec{\tau}_1, \quad \text{and} \quad \vec{\tau}_\omega(1) = 0$$

and `line 71:` $R = I$. Each iteration of the accumulation loop generates the PMD vectors from

`line 96:` $$\vec{\tau}(k) = \vec{\tau}_k + R_k\vec{\tau}(k-1)$$

`line 99:` $$\vec{\tau}_\omega(k) = \vec{\tau}_k \times \vec{\tau}(k) + R_k\vec{\tau}_\omega(k-1)$$

Note that the running product of `line 93:` $R(k) = R_kR(k-1)$ is recorded. This operator is used to find the input PSP's from the output PSP's. In particular,

`lines 104-106:` $$\vec{\tau}_s = R^\dagger\vec{\tau}_t, \quad \text{and} \quad \vec{\tau}_{s\omega} = R^\dagger\vec{\tau}_{t\omega}$$

With these preliminary calculations in place, the vector and scalar PMD spectra are computed on `lines 109-116`, following (C.1-C.2).

Figures C.1-C.2 are calculated for four equal-length stages using the above code fragment. The input and output PSP vector spectra are shown as are the DGD, magnitude SOPMD, and PDCD scalar spectra. The DGD spectra in Fig. 8.33 on page 362 were calculated in the same way.

Not included in the code but easily added is the calculation of $U(\omega)$. Direct calculation of $U(\omega)$ is ideal due to the difficulty extracting U from $jU_\omega U^\dagger$. While calculating $U(\omega)$ one should concurrently calculate $U_\omega(\omega)$ so that $jU_\omega U^\dagger$ can be checked against $\vec{\tau}\cdot\vec{\sigma}$, the latter being calculated from concatenation rules on $\vec{\tau}$ by R as above. The product rule for $U(\omega)$ is trivial:

$$U(N) = U_N U_{N-1} \ldots U_1 \tag{C.4}$$

The frequency derivative is calculated analytically and accumulated using a recurrence relation. Matrices U and U_ω are expressed as

$$U_k = I\cos(\omega\tau_k/2) - j\,(\vec{\tau}_k\cdot\vec{\sigma})\sin(\omega\tau_k/2) \tag{C.5a}$$

$$U_{\omega k} = -\tau_k/2\;\left(I\sin(\omega\tau_k/2) + j\,(\vec{\tau}_k\cdot\vec{\sigma})\cos(\omega\tau_k/2)\right) \tag{C.5b}$$

As with R_k, $\vec{\tau}_k\cdot\vec{\sigma}$, $\sin(\omega\tau_k/2)$, and $\cos(\omega\tau_k/2)$ can be calculated in advance of the frequency loop. The recurrence relation for $U_\omega(k)$ is

$$U_\omega(k) = U_{\omega k}U(k-1) + U_k U_\omega(k-1) \tag{C.6}$$

A quick test to verify that U and U_ω are correctly calculated is to check that $jU_\omega U^\dagger$ is Hermitian.

Calculation of $U(\omega)$ is useful, for instance, when calculating the time response of a signal that transits a PMD medium. The polarization transfer matrix in frequency and time domains are given by (8.2.41) and (8.2.42) on page 343.

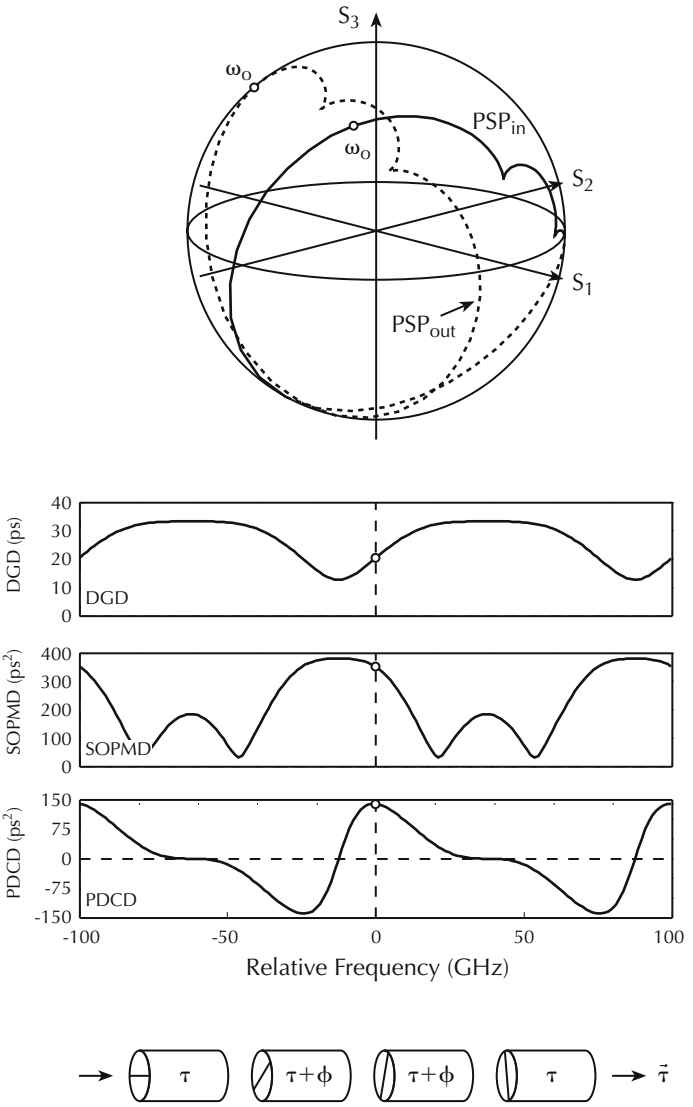

Fig. C.1. Vector and scalar spectra for four birefringent sections: $\tau = \{10, 10, 10, 10\}$ ps, $\phi = \{0, 45, 45, 0\}^\circ$, $\hat{r} = \{0, -45, -90, -135\}^\circ \times 1.5$ lying on the equator. The center frequency ω_o is indicated on both vector and scalar plots. The period of the scalar spectra is 100 GHz and the spectra have been shifted by one-eighth period.

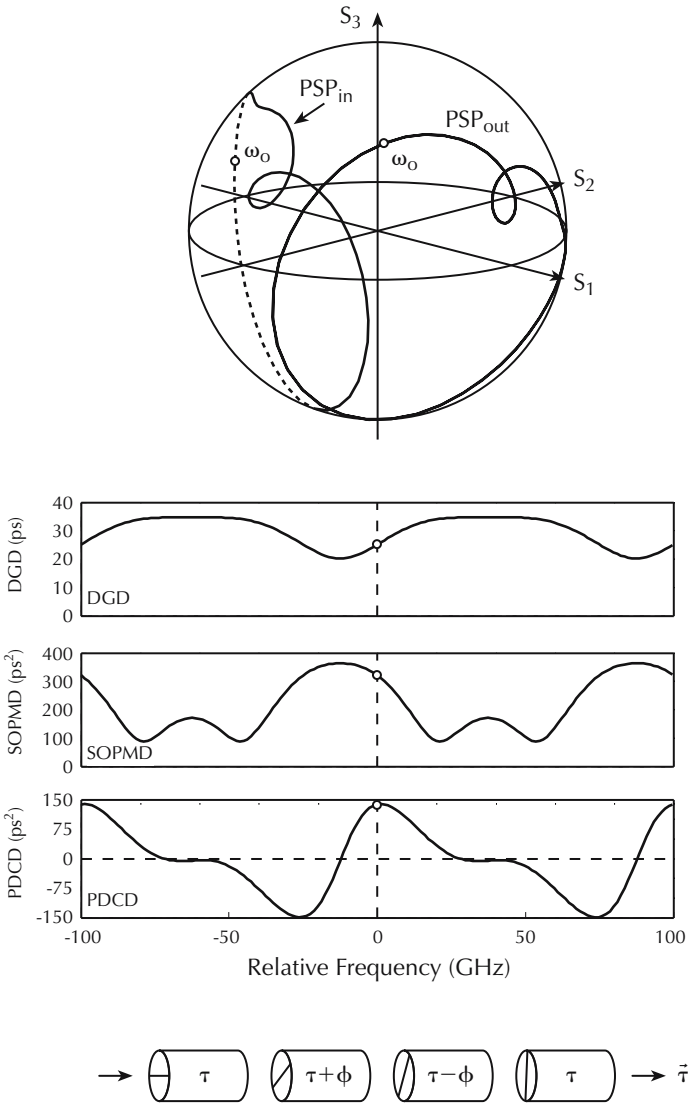

Fig. C.2. Vector and scalar spectra for four birefringent sections: $\tau = \{10, 10, 10, 10\}$ ps, $\phi = \{0, 22.5, 67.5, 0\}^\circ$, $\hat{r} = \{0, -45, -90, -135\}^\circ \times 1.25$ lying on the equator. The center frequency ω_o is indicated on both vector and scalar plots. The differential phase shift of 22.5° in the center sections about the common phase shift 45° distorts the PMD spectra.

D

Multidimensional Gaussian Deviates

Consider the gaussian random variable X. The probability density is

$$\rho_X(x) = \frac{1}{\sqrt{2\pi\sigma_x^2}} \exp\left(-\frac{x^2}{2\sigma_x^2}\right) \tag{D.1}$$

The expectation and variance are

$$E[X] = 0, \quad \text{and} \quad \text{var}(X) = \sigma_x^2 \tag{D.2}$$

Consider now a two-dimensional distribution composed of two independent identically distributed (i.i.d.) gaussian random variables (g.r.v.); denote the two deviates X_1 and X_2, and a vector defined as $\mathbf{X} = (X_1, X_2)$. While we may be interested in the distribution of these cartesian components, an alternative is the distribution of the corresponding polar coordinates. A polar deviate is defined as $\mathbf{P} = (R, \theta)$. A one-to-one map g relates the two coordinates such that

$$\begin{aligned} g(x_1, x_2) &= (r, \theta) \\ &= \left(\sqrt{x_1 + x_2}, \tan^{-1} x_2/x_1\right) \end{aligned}$$

The inverse map $h = g^{-1}$ given in polar form is

$$\begin{aligned} h(r, \theta) &= (x_1, x_2) \\ &= (r\cos\theta, r\sin\theta) \end{aligned}$$

The joint density of the polar coordinates is related to the joint density of the cartesian coordinates through the Jacobian:

$$\rho_{\mathbf{P}}(r, \theta) = \rho_{\mathbf{X}}(h(r, \theta)) J_h \tag{D.3}$$

where

$$J_h = \begin{vmatrix} \dfrac{\partial h_1}{\partial r} & \dfrac{\partial h_1}{\partial \theta} \\ \dfrac{\partial h_2}{\partial r} & \dfrac{\partial h_2}{\partial \theta} \end{vmatrix} \tag{D.4}$$

In the present case, $J_h = r$. The polar joint distribution is therefore

$$\rho_{\mathbf{P}}(r,\theta) = \frac{r}{2\pi\sigma_x^2}\ \exp\left(-\frac{r^2}{2\sigma_x^2}\right)$$

where the argument of the exponential is $x_1^2 + x_2^2 = r^2(\cos^2\theta + \sin^2\theta)$. Now, the random variables R and θ are independent, so the joint distribution is the product of the two individual distributions. The angular distribution is uniform over 2π, so the product is written as

$$\rho_\theta(\theta)\rho_R(r) = \left(\frac{1}{2\pi}\right)\left(\frac{r}{\sigma_x^2}\ \exp\left(-\frac{r^2}{2\sigma_x^2}\right)\right)$$

The resultant radial distribution, known at the Rayleigh distribution, is

$$\rho_R(r) = \frac{r}{\sigma_x^2}\ \exp\left(-\frac{r^2}{2\sigma_x^2}\right), \quad r \geq 0 \tag{D.5}$$

The moments of the Rayleigh distribution are

$$E\left[\rho_R^n(r)\right] = 2^{n/2}\sigma_x^n\Gamma\left(1+\frac{n}{2}\right), \quad n \in \mathbb{Z}$$

where $\mathbb{Z}$ is the set of integers greater or equal to zero. Denoting the n^{th} moment as $\langle r^n \rangle$ and $\text{var}\,(r) = \sigma_r^2$, the basic Rayleigh distribution parameters are

$$\langle r \rangle = \sqrt{\frac{\pi}{2}}\,\sigma_x, \quad \left\langle r^2 \right\rangle = 2\sigma_x^2 \tag{D.6a}$$

$$\sigma_r^2 = \left(2 - \frac{\pi}{2}\right)\sigma_x^2 \tag{D.6b}$$

Note in particular the relation between the first and second moments:

$$\left\langle r^2 \right\rangle = \frac{4}{\pi}\left\langle r \right\rangle^2 \tag{D.7}$$

Next consider the three-dimensional distribution of three i.i.d. gaussian random variables $\mathbf{X} = (X_1, X_2, X_3)$, each with variance σ_x^2, and its polar equivalent $\mathbf{P} = (R, \theta, \phi)$. In the polar coordinate system, $\theta \in [0, \pi]$ is the declination angle from X_3 and $\phi \in [-\pi, \pi]$ is the azimuth angle. The polar to cartesian transformation h is

$$\begin{aligned} h(r,\theta,\phi) &= (x_1, x_2, x_3) \\ &= (r\cos\phi\sin\theta, r\sin\phi\sin\theta, r\cos\theta) \end{aligned}$$

Table D.1. Key Relations for Multivariate Gaussian Distributions

Distribution	$\rho_R(r)$	$\langle r \rangle$	$\langle r^2 \rangle$	var (r)	ratio
Gaussian$^{(a)}$	$\dfrac{1}{\sqrt{2\pi\sigma_x^2}} \exp\left(-\dfrac{r^2}{2\sigma_x^2}\right)$	0	σ_x^2	σ_x^2	
Rayleigh$^{(b)}$	$\dfrac{r}{\sigma_x^2} \exp\left(-\dfrac{r^2}{2\sigma_x^2}\right)$	$\sqrt{\dfrac{\pi}{2}}\,\sigma_x$	$2\sigma_x^2$	$\left(2-\dfrac{\pi}{2}\right)\sigma_x^2$	$\langle r^2 \rangle = \dfrac{4}{\pi}\langle r \rangle^2$
Maxwellian$^{(b)}$	$\sqrt{\dfrac{2}{\pi}}\dfrac{r^2}{\sigma_x^3} \exp\left(-\dfrac{r^2}{2\sigma_x^2}\right)$	$\sqrt{\dfrac{8}{\pi}}\,\sigma_x$	$3\sigma_x^2$	$\left(3-\dfrac{8}{\pi}\right)\sigma_x^2$	$\langle r^2 \rangle = \dfrac{3\pi}{8}\langle r \rangle^2$

$^{(a)}$ $r \in (-\infty, \infty)$, $^{(b)}$ $r \in [0, \infty)$

The corresponding Jacobian is

$$J_h = r \sin\theta$$

The polar joint distribution $\rho_{\mathbf{P}}(R, \theta, \phi)$, written as the product of three independent polar random variables, is

$$\rho_\phi(\phi)\rho_\theta(\theta)\rho_R(r) = \left(\frac{1}{2\pi}\right)\left(\frac{\sin\theta}{2}\right)\left(\sqrt{\frac{\pi}{2}}\,\frac{r^2}{\sigma_x^3} \exp\left(-\frac{r^2}{2\sigma_x^2}\right)\right)$$

The resultant radial distribution, known at the Maxwellian distribution, is

$$\rho_R(r) = \sqrt{\frac{\pi}{2}}\,\frac{r^2}{\sigma_x^3} \exp\left(-\frac{r^2}{2\sigma_x^2}\right) \tag{D.8}$$

The moments of the Maxwellian distribution are

$$E\left[\rho_R^n(r)\right] = \frac{2}{\sqrt{\pi}}\, 2^{n/2}\sigma_x^n \Gamma\left(\frac{3+n}{2}\right)$$

Therefore, the basic parameters of the Maxwellian distribution are

$$\langle r \rangle = \sqrt{\frac{8}{\pi}}\,\sigma_x, \quad \langle r^2 \rangle = 3\sigma_x^2 \tag{D.9a}$$

$$\sigma_m^2 = \left(3 - \frac{8}{\pi}\right)\sigma_x^2 \tag{D.9b}$$

The relation between the first and second moments is

$$\langle r^2 \rangle = \frac{3\pi}{8}\langle r \rangle^2 \tag{D.10}$$

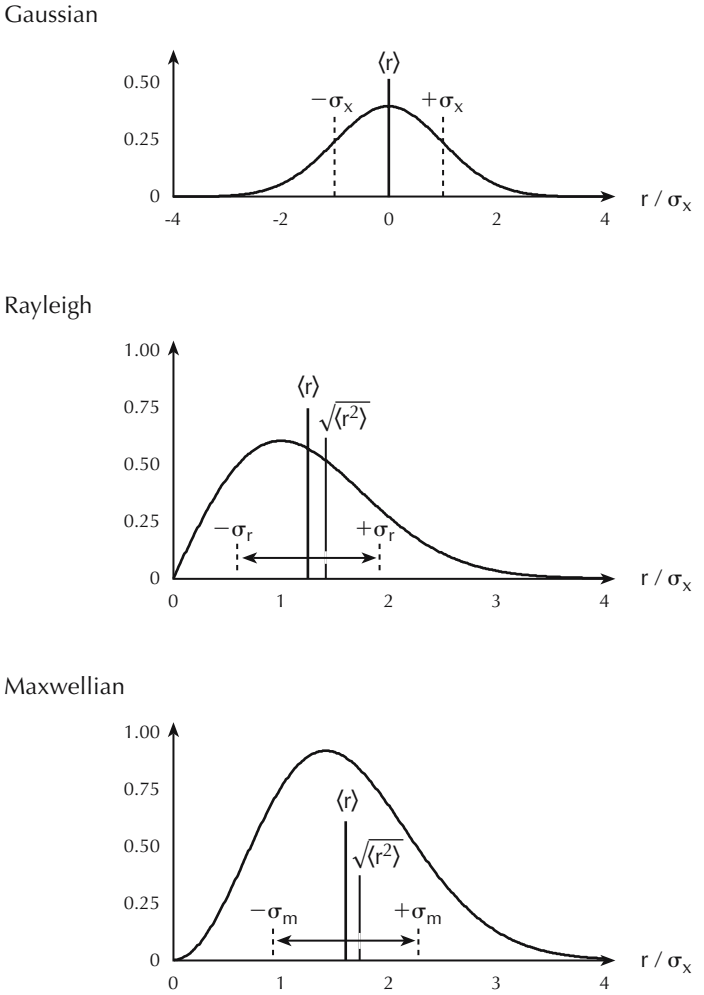

Fig. D.1. Probability densities for Gaussian, Rayleigh, and Maxwellian distributions. The gaussian distribution is symmetric about the origin while the Rayleigh and Maxwellian distributions, associated with the radius of a circle and sphere, respectively, are one-sided with $r \geq 0$. All distributions are completely determined by the component variance σ_x^2.

Index

Springer Series in

OPTICAL SCIENCES

Volume 1

1 **Solid-State Laser Engineering**
By W. Koechner, 5th revised and updated ed. 1999, 472 figs., 55 tabs., XII, 746 pages

Published titles since volume 80

80 **Optical Properties of Photonic Crystals**
By K. Sakoda, 2nd ed., 2004, 107 figs., 29 tabs., XIV, 255 pages

81 **Photonic Analog-to-Digital Conversion**
By B.L. Shoop, 2001, 259 figs., 11 tabs., XIV, 330 pages

82 **Spatial Solitons**
By S. Trillo, W.E. Torruellas (Eds), 2001, 194 figs., 7 tabs., XX, 454 pages

83 **Nonimaging Fresnel Lenses**
Design and Performance of Solar Concentrators
By R. Leutz, A. Suzuki, 2001, 139 figs., 44 tabs., XII, 272 pages

84 **Nano-Optics**
By S. Kawata, M. Ohtsu, M. Irie (Eds.), 2002, 258 figs., 2 tabs., XVI, 321 pages

85 **Sensing with Terahertz Radiation**
By D. Mittleman (Ed.), 2003, 207 figs., 14 tabs., XVI, 337 pages

86 **Progress in Nano-Electro-Optics I**
Basics and Theory of Near-Field Optics
By M. Ohtsu (Ed.), 2003, 118 figs., XIV, 161 pages

87 **Optical Imaging and Microscopy**
Techniques and Advanced Systems
By P. Török, F.-J. Kao (Eds.), 2003, 260 figs., XVII, 395 pages

88 **Optical Interference Coatings**
By N. Kaiser, H.K. Pulker (Eds.), 2003, 203 figs., 50 tabs., XVI, 504 pages

89 **Progress in Nano-Electro-Optics II**
Novel Devices and Atom Manipulation
By M. Ohtsu (Ed.), 2003, 115 figs., XIII, 188 pages

90/1 **Raman Amplifiers for Telecommunications 1**
Physical Principles
By M.N. Islam (Ed.), 2004, 488 figs., XXVIII, 328 pages

90/2 **Raman Amplifiers for Telecommunications 2**
Sub-Systems and Systems
By M.N. Islam (Ed.), 2004, 278 figs., XXVIII, 420 pages

91 **Optical Super Resolution**
By Z. Zalevsky, D. Mendlovic, 2004, 164 figs., XVIII, 232 pages

92 **UV-Visible Reflection Spectroscopy of Liquids**
By J.A. Räty, K.-E. Peiponen, T. Asakura, 2004, 131 figs., XII, 219 pages

93 **Fundamentals of Semiconductor Lasers**
By T. Numai, 2004, 166 figs., XII, 264 pages

Springer Series in

OPTICAL SCIENCES

94 **Photonic Crystals**
Physics, Fabrication and Applications
By K. Inoue, K. Ohtaka (Eds.), 2004, 209 figs., XV, 320 pages

95 **Ultrafast Optics IV**
Selected Contributions to the 4th International Conference
on Ultrafast Optics, Vienna, Austria
By F. Krausz, G. Korn, P. Corkum, I.A. Walmsley (Eds.), 2004, 281 figs., XIV, 506 pages

96 **Progress in Nano-Electro Optics III**
Industrial Applications and Dynamics of the Nano-Optical System
By M. Ohtsu (Ed.), 2004, 186 figs., 8 tabs., XIV, 224 pages

97 **Microoptics**
From Technology to Applications
By J. Jahns, K.-H. Brenner, 2004, 303 figs., XI, 335 pages

98 **X-Ray Optics**
High-Energy-Resolution Applications
By Y. Shvyd'ko, 2004, 181 figs., XIV, 404 pages

99 **Few-Cycle Photonics and Optical Scanning Tunneling Microscopy**
Route to Femtosecond Ångstrom Technology
By M. Yamashita, H. Shigekawa, R. Morita (Eds.) 2005, 241 figs., XX, 393 pages

100 **Quantum Interference and Coherence**
Theory and Experiments
By Z. Ficek and S. Swain, 2005, 178 figs., approx. 432 pages

101 **Polarization Optics in Telecommunications**
By J. Damask, 2005, 110 figs, XVI, 528 pages

102 **Lidar**
Range-Resolved Optical Remote Sensing of the Atmosphere
By C. Weitkamp (Ed.), 161 figs., approx. 416 pages

103 **Optical Fiber Fusion Splicing**
By A. D. Yablon, 2005, 100 figs., approx. 300 pages

104 **Optoelectronics of Molecules and Polymers**
By A. Moliton, 2005, 200 figs., approx. 460 pages

105 **Solid-State Random Lasers**
By M. Noginov, 2005, 149 figs., approx. 380 pages

106 **Coherent Sources of XUV Radiation**
Soft X-Ray Lasers and High-Order Harmonic Generation
By P. Jaeglé, 2005, 150 figs., approx. 264 pages

107 **Optical Frequency-Modulated Continuous-Wave (FMCW) Interferometry**
By J. Zheng, 2005, 137 figs., approx. 250 pages

108 **Laser Resonators and Beam Propagation**
Fundamentals, Advanced Concepts and Applications
By N. Hodgson and H. Weber, 2005, 497 figs., approx. 790 pages